Studying the phosphoryl transfer mechanism of the *E. coli* phosphofructokinase-2: From x-ray structure to quantum mechanics/molecular mechanics simulations.

Juliana Murillo–López,[‡a] *Kirill Zinovjev,*[‡b] *Humberto Pereira,*[c] *Andres Caniuguir,*[d] *Richard Garratt,*[c] *Jorge Babul,*[d] *Rodrigo Recabarren,*[a] *Jans Alzate-Morales,*[a] *Julio Caballero,**[a] *Iñaki Tuñón,**[b] *Ricardo Cabrera**[d]

[a] Centro de Bioinformática y Simulación Molecular (CBSM), Facultad de Ingeniería, Universidad de Talca, 1 Poniente 1141, Talca, Chile

[b] Departament de Química Física, Universitat de València, 46100 Burjassot, Spain

[c] Instituto de Física de São Carlos, Universidade de São Paulo, São Paulo, Brazil.

[d] Departamento de Biología, Facultad de Ciencias, Universidad de Chile, Santiago, Chile

Table of Contents

1. Proposed mechanism for Pfk-2.

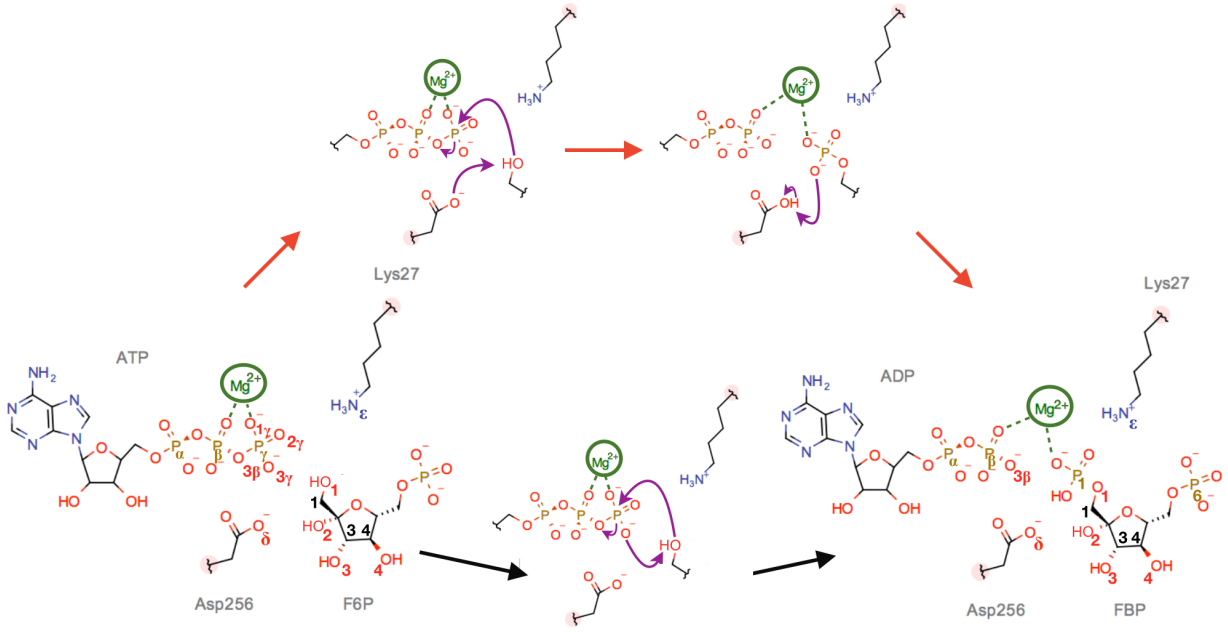

Fig. S1. Proposed mechanisms for Pfk-2. The upper mechanism is designed as an analogue of the mechanism suggested for D-tagatose-6-phosphate kinase reported by Miallau.[1] The mechanism below is based on the mechanism proposed for other kinases.

2. Crystallization, Data Collection, Structure Determination and Refinement.

The enzyme was purified as described by Parducci *et al*. (2006).[2] Crystals were grown by the vapor diffusion method in a hanging drop consisting of 2 μL of the protein stock solution (6 mg/ml of protein in 25 mM Tris-HCl pH 7.6 buffer, 10 mM $MgCl_2$, 30 mM dithiotreitol, and 6 mM ADP plus 6 mM FBP) of a reservoir solution comprising 21% PEG 4000, 0.1 M sodium acetate pH 4.75 and 0.2 M ammonium acetate. X-ray diffraction data were collected at 100 K on the W01B-MX2 LNLS beamline (λ = 1.45 Å) using a Marmosaic 225 CCD detector, over 1° increments of φ for a total rotation of 120° up to 2.0 Å resolution. The data were indexed, integrated, and scaled using the program XDS.[3] The structure of *E. coli* Pfk-2 in complex with the reactants (F6P and $MgATP^{2-}$) and the inhibitor $MgATP^{2-}$ in one active site, and the products (FBP and $MgADP^{-}$) in the other active site, was solved by molecular replacement using the Phaser program[4] and a monomer of the previously solved Pfk-2 structure in complex with ATP as a search model (Protein Data Bank code 3CQD). Model refinement was carried out with Phenix[5] employing TLS parameters (which describes the rigid body motion of large groups of atoms using Translation, Libration, and Screw-rotation displacements) in the final stages of refinement. Model building was performed with COOT,[6] using σ_A-weighted $2F_o - F_c$ and $F_o - F_c$ electron density maps. A total of 682 water molecules were included using both COOT and Phenix. The F6P, FBP, ATP^{4-}, ADP^{3-} and Mg^{2+} ligands were added using COOT. In all cases, the behavior of R_{free} was used as the principal criterion for validating the refinement protocol, and the stereochemical quality of the model was evaluated with Procheck[7] and Molprobity.[8] Full statistics for data collection and refinement are summarized in Table S1.

Table S1 Data collection parameters and structure refinement statistics [a]

	PFK2
PDB ID	3UQD
Space Group	*C222*$_1$
Cell dimensions (Å)	
a	69.89
b	155.19
c	224.99
Detector	MarCCD 225
X-ray Source	LNLS- W01B-MX2
λ (Å)	1.459
Resolution range (Å)	19.79 – 2.14 (2.27-2.14)
$R_{meas\ (\%)}$	10.0 (62.5)
Multiplicity	3.67 (3.48)
Completeness (%)	96.3 (76.4)
Reflections	67552
Unique Reflections	3247
I/σ	1.54 (at 2.15 Å)
Refinement parameters	
Reflections used for Refinement	64934
R(%)**	19.5
R_{free}(%)**	25.5
N° of protein atoms	9057
N° of ligant atoms	225
B (Å^2)	32.1
Coordinate Error (ML based) (Å)	0.62
Phase error (°)	26.97
Ramachandran plot	
Favored (%)	93.1
Allowed (%)	6.3
Outliers (%)	0.2
All-atom Clashscore	4
RMSD from ideal geometry	
r.m.s. bond lengths (Å)	0.006
r.m.s. bond angles (°)	0.875

[a]The values in parentheses are for the outer resolution shells

3. General setup considerations.

3.1 System building. The system was prepared using the Protein Preparation Wizard application provided by Maestro in the Schrödinger Suite 2015.[9] Hydrogen atoms were added to the structure, and the complete system was checked to detect steric clashes or bad contacts. Protonation states of titratable residues at pH 7 were determined using PROPKA.[10] Protonation states were also manually inspected to optimize hydrogen-bond networks. To setup the system for MD simulations, the protein complex was embedded in an orthorhombic water box 113 x 76 x 75 Å in size using the SPC[11] water model, keeping a buffer region of approximately 10 Å around the protein in all directions. Sodium ions were added to neutralize the system. The final system was composed of two Pfk-2 subunits (309 residues per chain), both reactants (F6P, ATP^{4-}) both products (FBP, ADP^{3-}), one Mg^{2+} ion per subunit, 22 sodium ions, 11 crystallization water molecules, and 19300 solvation water molecules. A total of 67279 atoms formed the final molecular model.

The protonation patterns of all histidine residues in the system are collected on Table S2. Also we add information of any anomalous protonation state during the system setup.

Table S2 Special protonation states

Amino Acid	*Chain*	*Protonation State*
His50	B	Double protonated
His68	B	Delta
His94	B	Epsilon
His96	B	Epsilon
His297	B	Delta
His50	D	Delta
His68	D	Epsilon
His94	D	Epsilon
His96	D	Epsilon
His297	D	Double protonated
Asp256 (Prod)	B	Protonated

3.2 MD Simulations. Classical MD simulations were performed with Desmond 3.8[12,13] using the OPLS_2005 all-atom force field.[14,15] The system was equilibrated using the default protocol implemented in Desmond. This protocol consists of two minimizations using a steepest-descent algorithm with and without restraints on solute heavy atoms, followed by 60 fs MD simulation at 300K and 1 atm (according to the "quick relaxation" protocol in the Maestro interface of Desmond). Next, 12 ps MD simulation using the NVT ensemble followed by 12 ps NPT MD simulation with restraints on solute heavy atoms using a force constant of 50 kcal•mol^{-1}•Å^{-2} and a temperature of 10 K were performed. Then, the temperature was gradually increased to 300 K and the simulations were performed without restraints for 12 ps and 24 ps on each ensemble, respectively. After system equilibration, we performed 100 ns of fully unrestrained MD simulation using NPT ensemble. The temperature was maintained using a Nosé-Hoover chain thermostat[16] with a relaxation time of 1 ps. Pressure was held constant by the Martyna-Tobias-Klein barostat[17] using isotropic coupling with a relaxation time of 2 ps. Long-range electrostatic interactions were computed using the particle mesh Ewald[18] method. Lennard-Jones (LJ) and short-range electrostatic interactions were calculated at every step using a smooth switching function with a 9 Å cutoff. Integration of the motion equations was carried out by the RESPA (time-reversible reference system propagator algorithm)[19] scheme using 2 fs for bonded and short-range non-bonded interactions and a 6 fs time-step for long-range electrostatic interactions. Constraints for the X-H bonds were implemented by the M-SHAKE algorithm.[20] The total simulation time was distributed in 10 ns of further stabilization and 90 ns for production dynamics, with the latter being used for analysis.

3.3 QM/MM Calculations. The selected QM subsystem (88 atoms in total) was composed of F6P, ATP^{4-}, one Mg^{2+} ion and the side-chains of all the residues that complete the Mg^{2+} coordination sphere (3 coordinating water molecules and the Asp166 residue). In addition, Asp256 together with the Lys27 residue from the complementary subunit were included to study the catalytic mechanism represented in Fig. 2 in the main manuscript (see Results and Discussion presented there). The QM region was described using the AM1/d-PhoT semi-empirical level of theory, which was specifically parameterized for H, O and P atoms involved in phosphoryl transfer reactions,[21,22] while the rest of the system was described by the OPLS force field implemented in fDynamo.[23,24] To saturate the valence of the QM/MM frontier atoms, the link atom procedure was used.[25,26] After the initial minimization, a 100 ps NVT MD simulation was performed using the hybrid QM/MM potential described above.

3.4 QM/MM Free Energy Calculations. The CVs selected to trace the MFEPs (represented in Fig. 2 in the main manuscript) are the distances between the carboxylate oxygen Oδ of residue Asp256 and the hydrogen at oxygen O1 of F6P d($O\delta_{(Asp256)}$: $H_{O1(F6P)}$), between the hydrogen at oxygen O1 of F6P and oxygen O1 of F6P d($H_{O1(F6P)}$: $O_{1(F6P)}$), between oxygen O1 of F6P and the Pγ phosphorus of ATP d($O_{1(F6P)}$: $P\gamma_{(ATP)}$), between the Pγ phosphorus of ATP and oxygen 3β of ATP d($P\gamma_{(ATP)}$: $O_3\beta_{(ATP)}$), and between the hydrogen at oxygen O1 of F6P and the 3γ oxygen of ATP ($H_{O1(F6P)}$: $O_3\gamma_{(ATP)}$). In addition, the last CV was the hybridization change of the transferred phosphorous atom Pγ (the list of CVs is also indicated in Fig. 1 in the main manuscript, at the right). It is worth noting that we considered different string initial guesses for each mechanism under study, which differed in the initial values of the CVs along the path. These values were selected considering the CV values for the starting structure of reactants and products, and choosing intermediate values for the possible TS depending on the sought mechanism. Two initial guesses converged to two different MFEPs (Path 1 and Path 2). For Path 1 we used 140 string nodes to follow the reaction until the product state (including the proton transfer from Asp256 to the phosphate group), whereas 100 string nodes were needed for Path 2. For each node, we performed 160 and 120 ps of Langevin dynamics at 300 K with a time step of 1 fs for Paths 1 and 2, respectively. The nodes of the string converged within the initial 20/70 ps of dynamics. The average positions of the nodes for the converged strings were determined over the last 80 and 30 ps in Paths 1 and 2, respectively. The force constant values employed in the string method were 3000 $kJ \cdot mol^{-1} \cdot Å^{-2}$ for the distances and 15000 $kJ \cdot mol^{-1} \cdot Å^{-2}$ for the hybridization coordinate, while the friction coefficient was set to 9000 ps^{-1}.

To obtain the PMFs, a set of 100 points was interpolated from the string nodes of Paths 1 and 2 to define the path CVs (the *s* coordinate) as described by Zinovjev *et. al*.[27] The path CVs measure the progress of the system from reactants to products along the MFEP and range from 0 to 1. The PMFs were obtained using umbrella sampling.[28] The system was constrained around given values of the *s* coordinate and a biasing parabolic potential, with a force constant that was constantly updated, was added to assure evenly distributed sampling. Each of the 140/100 simulation windows used to obtain the PMFs corresponding to Path 1/2 consisted of 160/120 ps of Langevin dynamics at 300 K with a time step of 1 fs. The same AM1d-PhoT/OPLS[21] potential used for the QM/MM MD simulations was employed to obtain the PMFs. The B3LYP/6-311++G**/OPLS[29–32] potential was used for *a posteriori* corrections by means of single point calculations on

optimized geometries along the path CV. Single point energies at the higher level of theory were obtained using Gaussian09[33] coupled to fDynamo.

When was required, the bond orders were calculated using the Pauling bond order equation:[34]

$$n_x = n_0 e^{\left(\frac{(r_0 - r_x)}{c}\right)}$$

where bond order n_x of a bond of length r_x is a function of a reference bond of length r_o, whose bond order is defined as n_o. We used the single bond P-O distance as a reference ($n_o = 1$, $r_o = 1.63$Å[35]) and chose $c = 0.6$ that is better for the analysis of bond orders in transition states.

Additional QM/MM calculations using fDynamo coupled to Gaussian09 were done in order to further support the preference of Path 1 over Path 2. For this, one representative structure of the string calculation that contains $O_{3\beta}$-P_γ and P_γ-$O_{1(F6P)}$ distances close to 2.9 Å was selected. This structure would correspond to a point in Fig. 5 for Path 1 where both bond orders have the same value (lower part of the plot, n~0.15). With this structure at hand, a QM/MM scan calculation at the B3LYP/6-31G* level was performed including the same atoms in the QM region as was done in the string calculation. Here, the donor-acceptor distance $O_{3\beta}$-$O_{1(F6P)}$ was constraint to different values which were gradually decreased by 0.05 Å. To maintain the phosphoryl group positioned between both donor and acceptor oxygen atoms, and additional coordinate (TRANSFER) implemented in fDynamo was used. This coordinate is the scalar product between a vector defined by the position of the phosphorous atom and the middle point between the donor and acceptor oxygen atoms and the normalized vector defining the donor-acceptor distance. Thus, it is the vector projection of the first vector on the second one. This coordinate restricts the phosphorous atom to stay between both donor and acceptor oxygen atoms. Therefore, as the donor-acceptor distance is reduced, the potential energy surface explored moves towards an associative mechanism, which would approximately resemble a point in Fig. 5 for Path 2 (upper part of the plot, n~0.42) where both bond orders have the same value. The scan was run for 30 points and the results are shown in Fig. S11.

4. Some relevant distance and energy values along the main text

Table S3 Relevant distances mentioned along the main text

Crystal Structure		
Chain	*Label*	*Distance (Å)*
D	$d(P_{(F6P)}:Cz_{(Arg29)})$	4.41
D	$d(P_{(F6P)}:Cz_{(Arg90)})$	4.39
B	$d(P_{2(FBP)}:Cz_{(Arg29)})$	4.56
B	$d(P_{2(FBP)}:Cz_{(Arg90)})$	4.19
D	$d(O_{3(F6P)}:O\delta_{(Asp14)})$	2.77
D	$d(O_{4(F6P)}:O\delta_{(Asp14)})$	2.80
B	$d(O_{3(FBP)}:O\delta_{(Asp14)})$	2.67
B	$d(O_{4(FBP)}:O\delta_{(Asp14)})$	2.76
D	$d(O_{1(F6P)}:O\delta_{(Asp256)})$	3.89
D	$d(O_{2(F6P)}:O\delta_{(Asp256)})$	3.68
B	$d(O_{1(FBP)}:O\delta_{(Asp256)})$	3.39
B	$d(O_{2(FBP)}:O\delta_{(Asp256)})$	3.79
D	$d(O_{1(F6P)}:Nz_{(Lys27)})$	3.10
D	$d(P_{(F6P)}:Nz_{(Lys27)})$	4.31
B	$d(O_{1(FBP)}:Nz_{(Lys27)})$	3.70
B	$d(P_{2(FBP)}:Nz_{(Lys27)})$	3.76
MD (100ns average)		$\mu \pm s$ *(Å)*
D	$d(P_{(F6P)}:Cz_{(Arg90)})$	4.00 ± 0.08
B	$d(P_{2(FBP)}:Cz_{(Arg90)})$	4.00 ± 0.07
D	$d(H_{O3(F6P)}:O\delta_{1(Asp14)})$	1.77 ± 0.23
D	$d(H_{O4(F6P)}:O\delta_{2(Asp14)})$	1.83 ± 0.30
B	$d(H_{O3(FBP)}:O\delta_{1(Asp14)})$	1.81 ± 0.25
B	$d(H_{O4(FBP)}:O\delta_{2(Asp14)})$	2.04 ± 0.91
D	$d(O_{1(F6P)}:C\gamma_{(Asp256)})$	3.31 ± 0.14
B	$d(O_{1(FBP)}:C\gamma_{(Asp256)})$	3.59 ± 0.25
D	$d(P\gamma_{(ATP)}:Nz_{(Lys27)})$	3.49 ± 0.20
B	$d(P_{1(FBP)}:Nz_{(Lys27)})$	3.74 ± 0.15
D	$d(O_{1(F6P)}:P\ \gamma_{(ATP)})$	5.27 ± 0.24
B	$d(P_{1(FBP)}:O_3\beta_{(ADP)})$	4.61 ± 0.42

QM/MM (Chain B)		
s=0 / Path 1	$d(O_{1(F6P)}:P\gamma_{(ATP)})$	5.73
s=0 / Path 2	$d(O_{1(F6P)}:P\ \gamma_{(ATP)})$	4.16
s=0.45 / Path 1	$d(O_{1(F6P)}:P\gamma_{(ATP)}) = d(P\gamma_{(ATP)}:O_3\beta_{(ATP)})$	2.85
s=0.6 / Path 1	$d(O\delta_{(Asp256)}:H_{O1(F6P)}) = d(H_{O1(F6P)}:O_{1(F6P)})$	1.31
s=0.3 / Path 2	$d(H_{O1(F6P)}:O_{1(F6P)}) = d(H_{O1(F6P)}:O_3\gamma_{(ATP)})$	1.34
s=0.5 / Path 2	$d(O\delta_{(Asp256)}:H_{O1(F6P)}) = d(H_{O1(F6P)}:O_{1(F6P)}$	2.76
s=0.75 / Path 2	$d(O_{1(F6P)}:\ P\gamma_{(ATP)}) = d(P\gamma_{(ATP)}:O_3\beta_{(ATP)}$	2.07

Table S4 Relevant activation free energies mentioned along the main text

Activation Free Energy values in kcal/mol		
Experimental value		15.2
Path 1	***A*** (AM1d-PhoT/OPLS)	27.0
Path 2	***A*** (AM1d-PhoT/OPLS)	35.2
Path 1	***A*** (B3LYP/6-311++G**/OPLS)	21.0
Path 2	***A*** (B3LYP/6-311++G**/OPLS)	55.2
Path 1	***A*** (B3LYP/6-311++G**/OPLS) + ZPE Correction	19.1

5. Analysis during the MD Simulations

5.1. A closed conformation is retained in the presence of products. Interactions in the active sites of each complex seem to depend on the relative orientations of the domains, which in turn could be affected by the presence of the inhibitor $MgATP^{2-}$, because it bridges the minor and major domains, stabilizing the overall conformation. The root-mean-square deviation (RMSD) for the Pfk-2 dimeric complex, shown in the Supporting Information (Fig. S2), indicates that the system is stable and does not show large conformational changes. The backbone_RMSD values obtained at the end of the simulation seems to be related mainly with helices and loops changes during the relaxation process. The main changes are presented in chain B as could be observed in the upper part of Fig S2. However, in order to assess changes in the level of compaction between both chains along the trajectory, we calculated the distance between the center of mass (COM) of the two domains (Fig. S3) using the VMD plug-in DisRg developed by Falsafi-Zadeh et al.[36] This distance was also determined for the different chains in 3CQD, 3N1C and 3UQD crystals, and the minimum and maximum values in each case were used to define the reference intervals shown in Fig. S3. When comparing COM distances in 3N1C and 3CQD, the first showed the most closed and open structures, and the second showed narrow values in the middle. However, the chains in the 3UQD structure cover higher values than observed for 3N1C. Interestingly, for the chains containing products in 3UQD had a COM distance shorter than observed for those containing the reactants. In the molecular simulation, the difference between both distances increased. In the subunit with reactants, the absence of the allosteric ATP led to an even greater distance (an average of 26.8 ± 0.2 Å, during the last 10 ns), in the subunit containing products, the distance between the COM of the major and minor domains decreased to an average of 25.9 ± 0.1 Å. Although the average is higher than the distance observed in the most compact subunit of 3N1C, instantaneous values fluctuated significantly and reached even shorter values. These results showed that in the complex of Pfk-2 containing reactants and products, a closed conformation is favored in the product-containing chain.

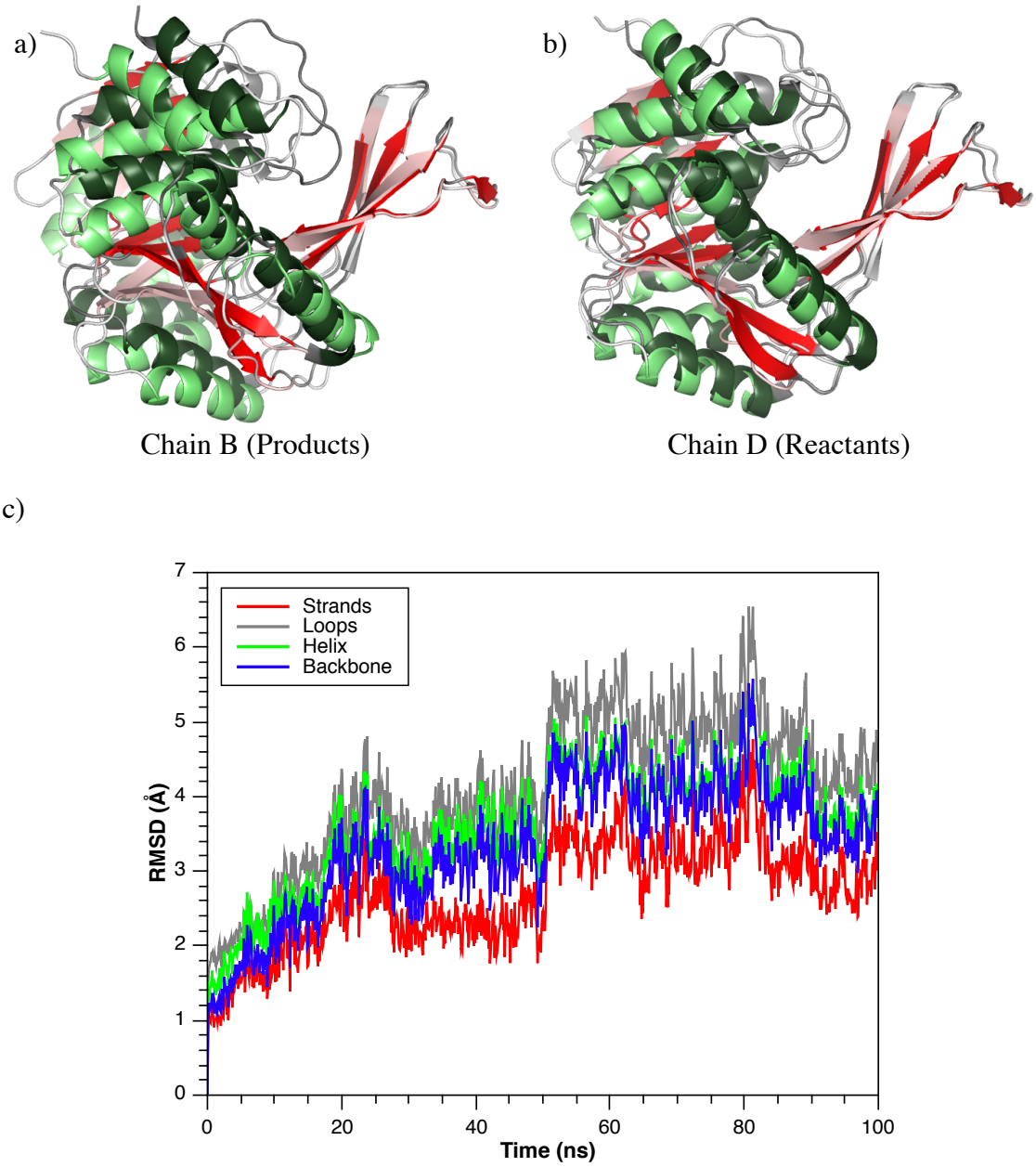

Fig. S2. Alignments of the structure of chains B (a) and D (b) obtained after the MD simulation with the corresponding chains in the crystallized tetramer (PDB code 3UQD). The strands are colored in red (3uqd) / light red (MD), helices are colored in green (3uqd) / light green (MD), and loops are colored in gray (3uqd) / light gray (MD). (c) RMSD of the 100ns MD simulation with respect to the crystal structure 3uqd. The strand, loops, helices and backbone RMSD are represented in red, gray, green and blue respectively as shown in the legend.

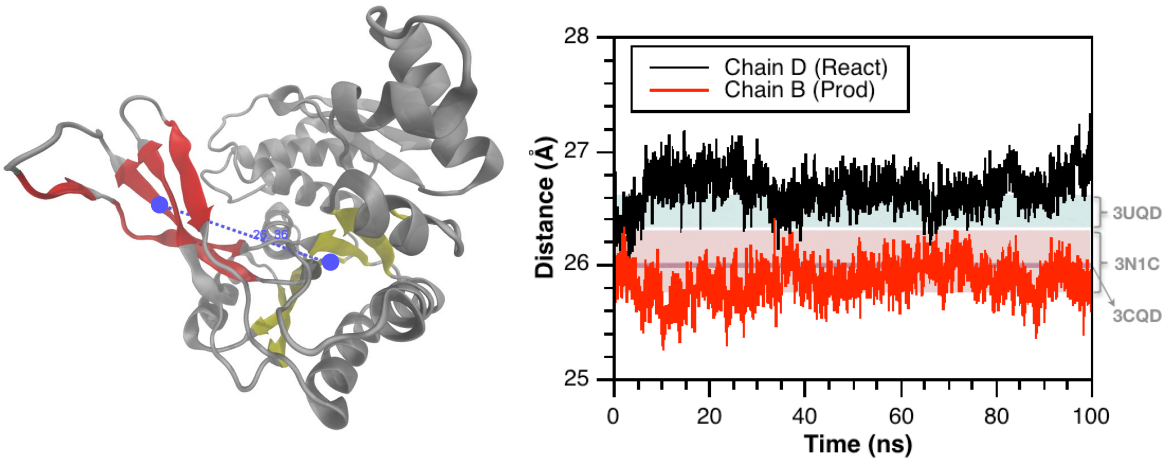

Fig. S3. Distance between the center of mass (COM) belonging to major and minor domains calculated on each chain along the classical molecular dynamics simulation. COM values were determined on β-sheets 2, 3a, 3b, 6 and 7 (in red) from the minor domain and 1, 4, 5, 8, 9, 10 (in yellow) from the major domain (according to Ref 28 in the main text) as shown in the upper figure. The shaded areas represent the range of minimum and maximum COM values from different Pfk-2 crystal structures.

5.2. Stability of the interactions between ligands and active site residues. Among the interactions established between ligands and residues in the active sites, some were very stable and others changed with respect to the crystal. Starting with the 6-phosphate moiety of the sugar, we observed a very stable network of interactions, where the ionic bridges made by Arg90 and Arg29 (from the complementary chain) play an important role. As an example, Fig. S4 depicts the variation of the distance between the central carbon atom of the guanidinium group of Arg90 (Cz) and the 6-phosphorus atom of F6P and FBP during MD simulations. It is clear that the affinity for the sugar-phosphate depends on the establishment of this network of interactions, as previously illustrated by the site-directed mutant Arg90Gln.[37] Additionally, the interactions of fructose hydroxyl groups OH3 and OH4 with the side chain carboxylate of residue Asp14 are important for the recognition of the sugar ring among phosphosugar kinases.[38] The time evolution of the distances associated to these interactions for both chains is shown in the upper part of Fig. S5. Despite the average distance between these hydroxyl groups and Asp14 is similar in both chains, larger fluctuations are observed in the simulation performed in chain B.

In the alignment of different protein-substrate complexes in the ribokinase family, all the hydroxymethyl groups of their substrates occupy the same location and are oriented in the same way,[39] forming an HB with a strictly conserved aspartate residue that belongs to the GXGD motif.[37,40] This conserved residue corresponds to Asp256 in Pfk-2. The lower part of Fig. S5 shows the difference in distance between this residue and the O1 atom of either F6P or FBP, showing the formation of a very stable interaction between them during the MD simulation. It is worth noting that during the system construction, the PROPKA[10] program determined that residue Asp256 in chain B should be protonated according to its chemical environment. Although FBP now has a phosphate group bonded to the sugar oxygen O1, the distance $O_{1(Sugar)}$-$C_{(Asp256)}$ remains almost the same in both chains, as depicted in Fig. S5c.

Fig. S6 shows the interaction between the amino group of Lys27 (from the adjacent subunit), and either the phosphate of $MgATP^{2-}$, or the 1-phosphate in FBP. The importance of the stable ionic interaction made by this residue has been discussed in the main manuscript. Other interactions that play a role not only for charge stabilization but also for a correct orientation of the phosphate moiety of the nucleotides (ADP or ATP) for catalysis occur with the β- and α-phosphates. The β-phosphate formed HB or electrostatic interactions with residues Lys185 and Asn187 mediated by a water molecule, whereas the α-phosphate group presents a stable HB interaction with Ser224. We plotted the relevant distances for these interactions in Fig. S7. Moving on to the chain that contains the products, we observed that the phosphate of ADP maintains interactions with residue Lys185, but here the hydroxyl

group of Ser224 is closer to the α-phosphate. The HB interaction between Asn187 and the β-phosphate was stable at the beginning of the MD simulation, and it remained stable until the helix (containing the residue) started to move away from the $MgADP^-$ ligand on chain B.

Regarding the environment around Mg^{2+} within the Pfk-2 active sites, Fig. S8 depicts the distance between the ion and the species involved in its coordination spheres. In both cases, the coordination sphere is composed of 6 oxygen atoms: one from the side chain carboxylate of Asp166, two from the groups of ATP (in the case of the reactants) or 1-phosphate from FBP and β-phosphate from ADP (in the case of the products), and three from water molecules. The distance to Asp166 is the shorter (1.9 Å in average) and it is not present in the crystal at any active site. Furthermore, in the case of the products, this residue enters the coordination sphere only after 10 ns of MD, replacing one water molecule. Interestingly, upon phosphoryl transfer, the equidistant interaction of Mg^{2+} with the oxygen atoms of γ- and β-phosphates (approximately 2.2 Å) changed to a configuration where the β-phosphate was closer to Mg^{2+} (1.9 Å in average) and the transferred phosphoryl was pushed apart, together with the three water molecules, which were located within a range between 2.5 and 3.0 Å in both active sites.

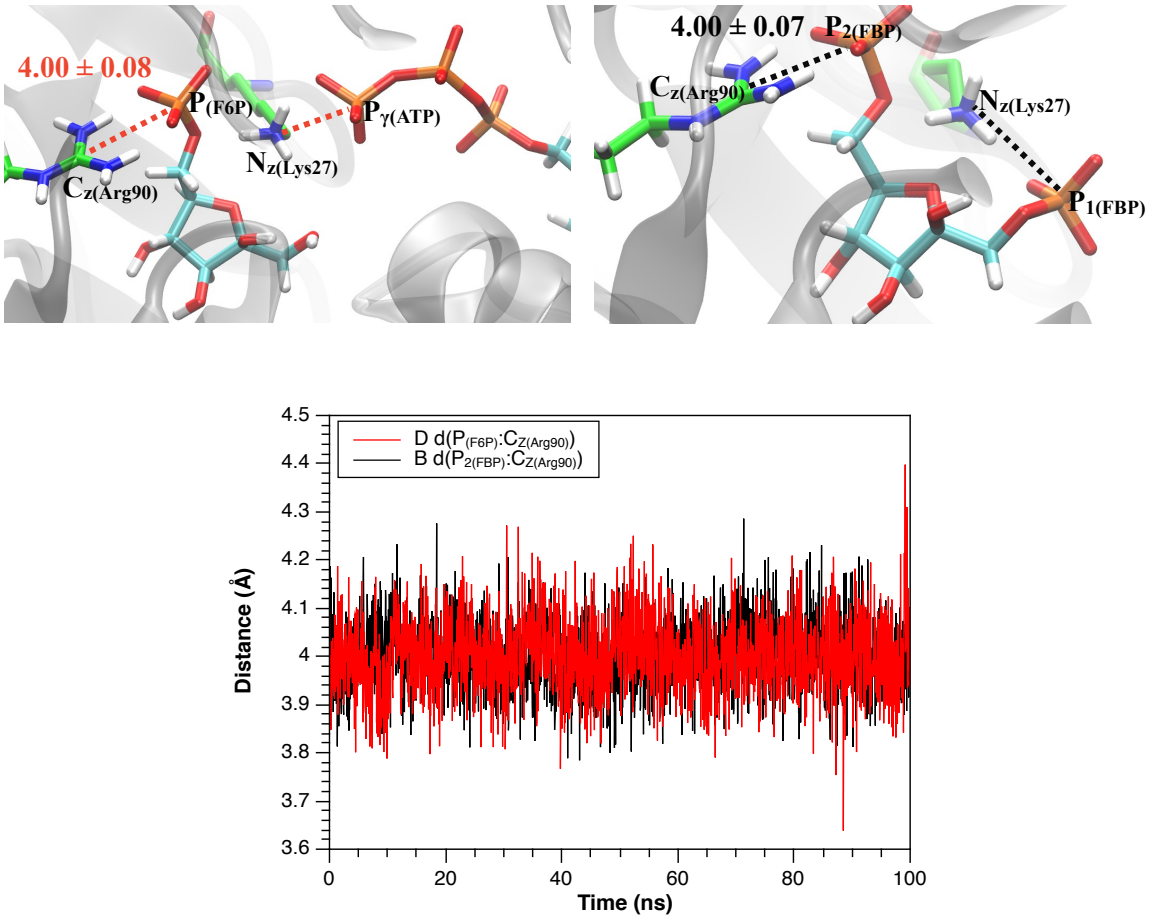

Fig. S4. Distances from the central phosphorus atom of the phosphosugar phosphate group, to the central guanidinium carbon atom from the conserved residue R90. They are calculated in both chains, which are represented by letter B and D. The average distances from the simulation are also depicted, using the same color as in the legend.

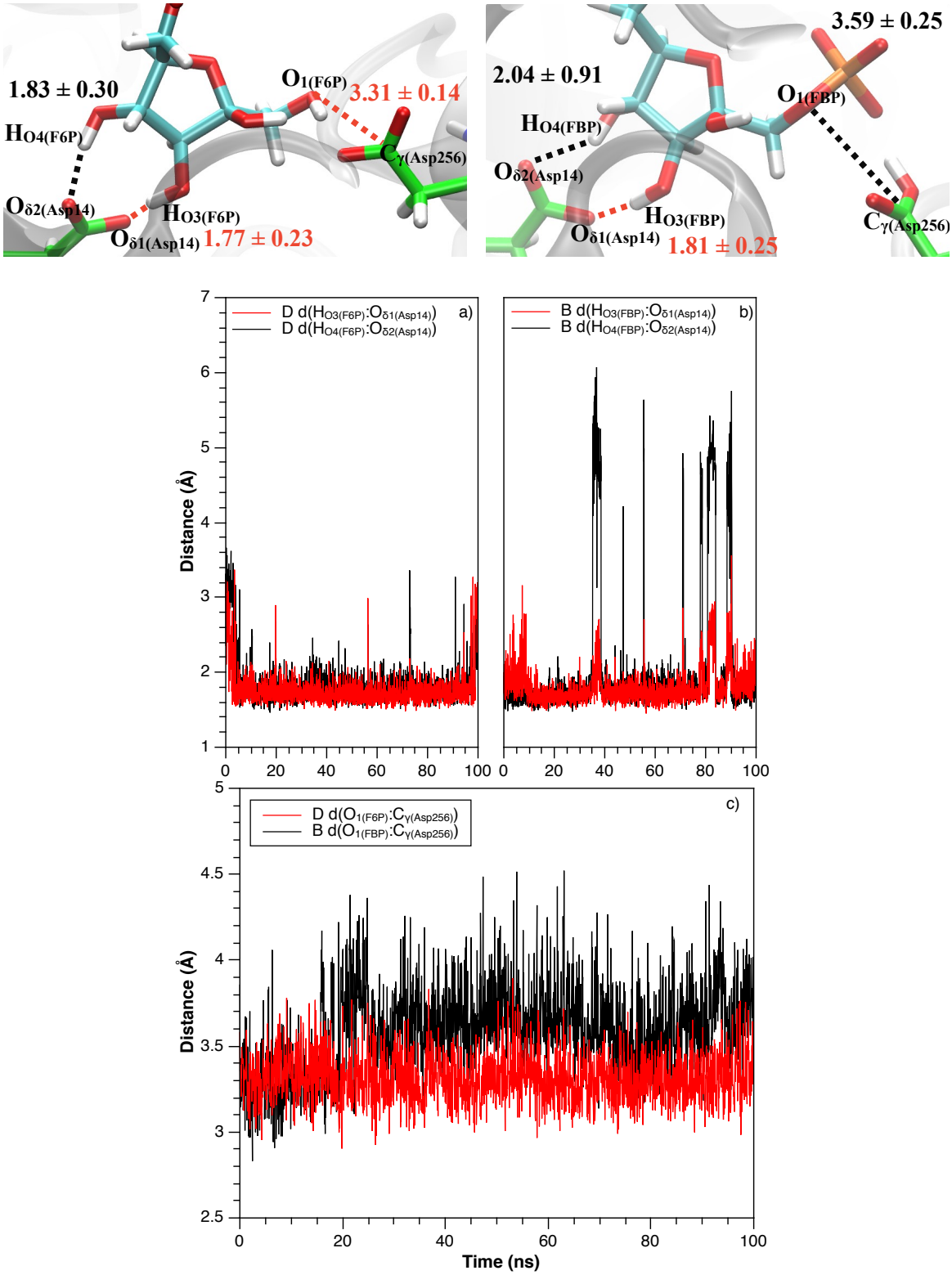

Fig. S5. Distances between the phosphosugar and the key aspartic residues: (a, b) Asp14 and (c) Asp256 in both chains. The chains are represented by letter B or D. Also the average distances from the simulation are depicted, using the same color as in the legend.

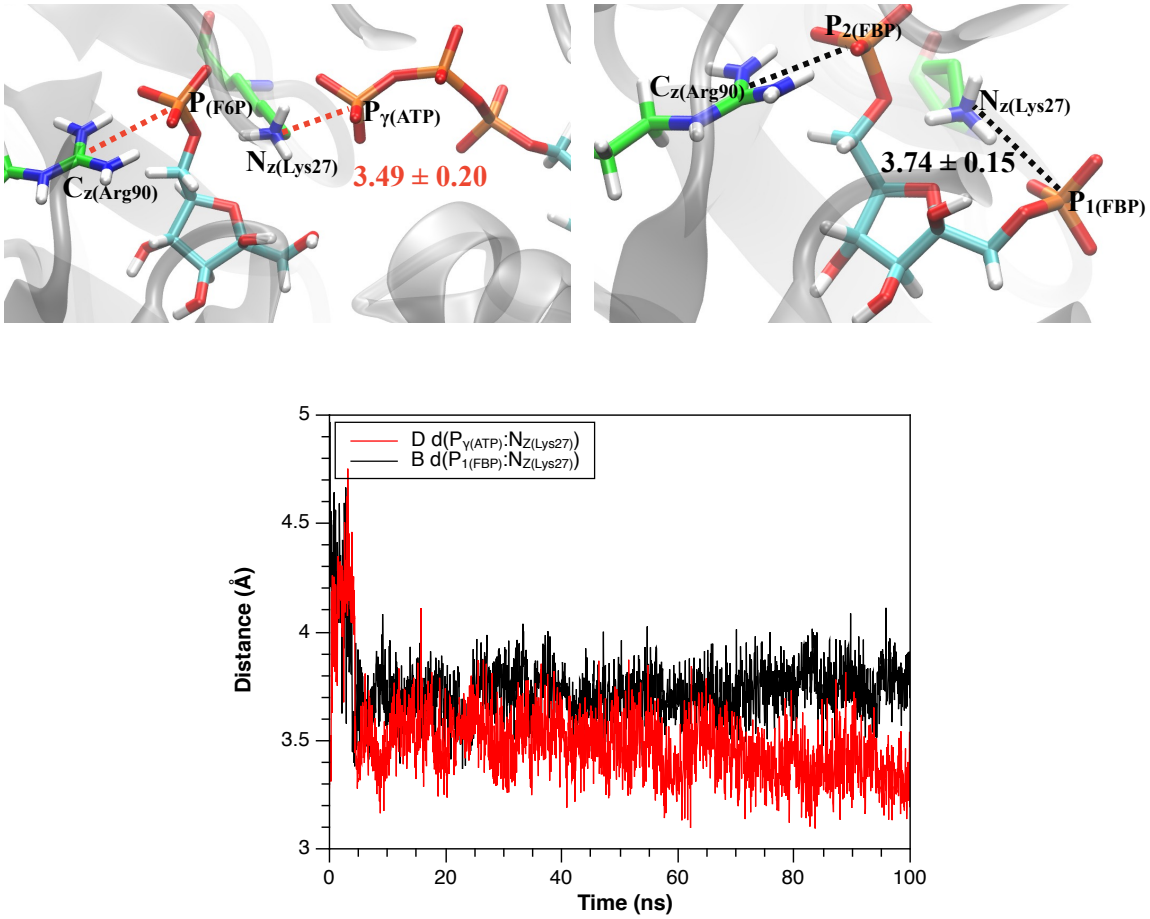

Fig. S6. Distances from the central phosphorus atom of the phosphosugar phosphate group, to the central nitrogen atom of the ε-amino group from residue K27. They are calculated in both chains, which are represented by letter B and D. The average distances from the simulation are also depicted, using the same color as in the legend.

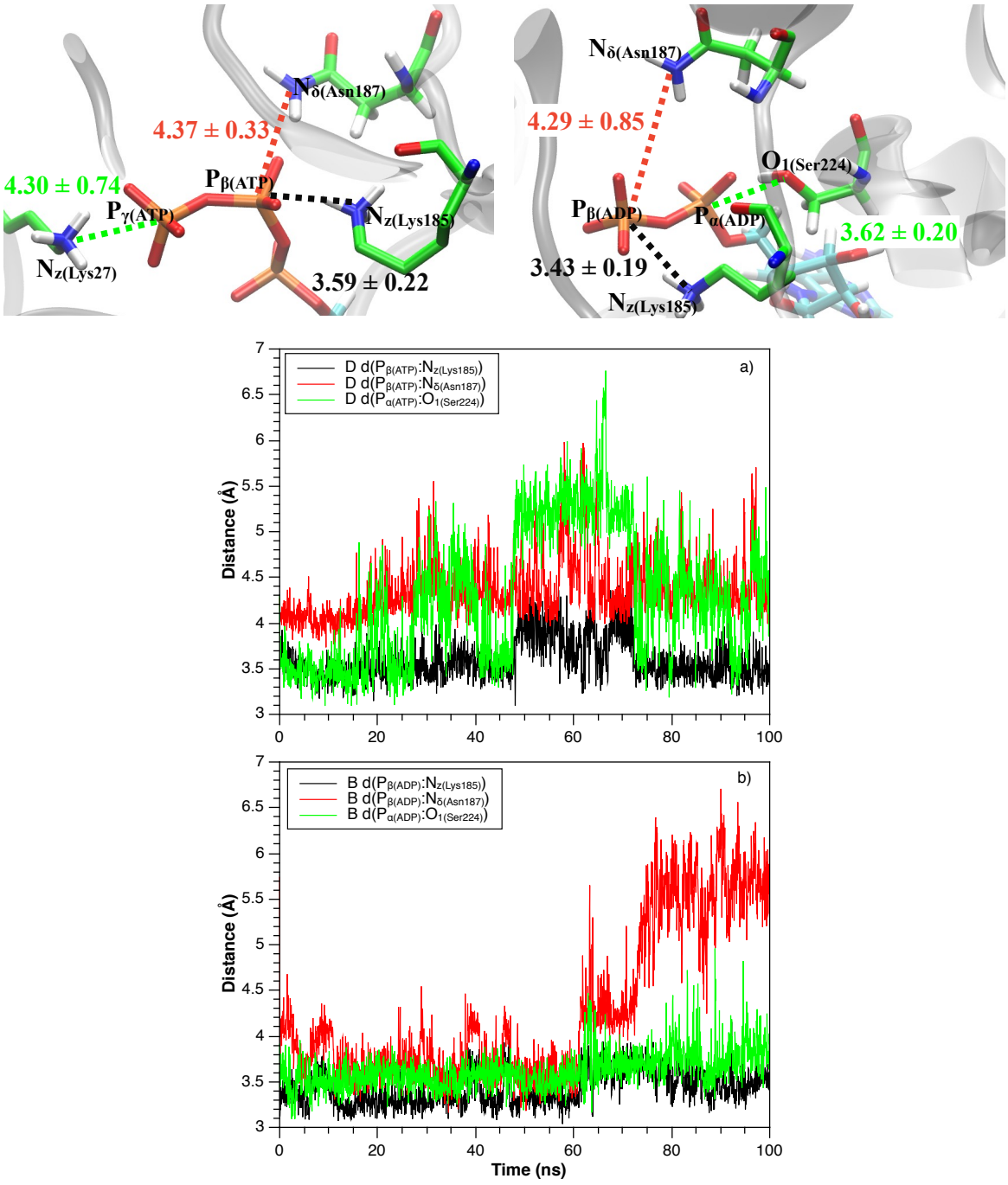

Fig. S7. Distances from the Mg-nucleotide phosphorus atoms to the residues in the vicinities for (a) the chain containing reactants and (b) the chain containing products. The chains are represented by letter B and D as in the text. The average distances from the simulation are also depicted, using the same color as in the legend.

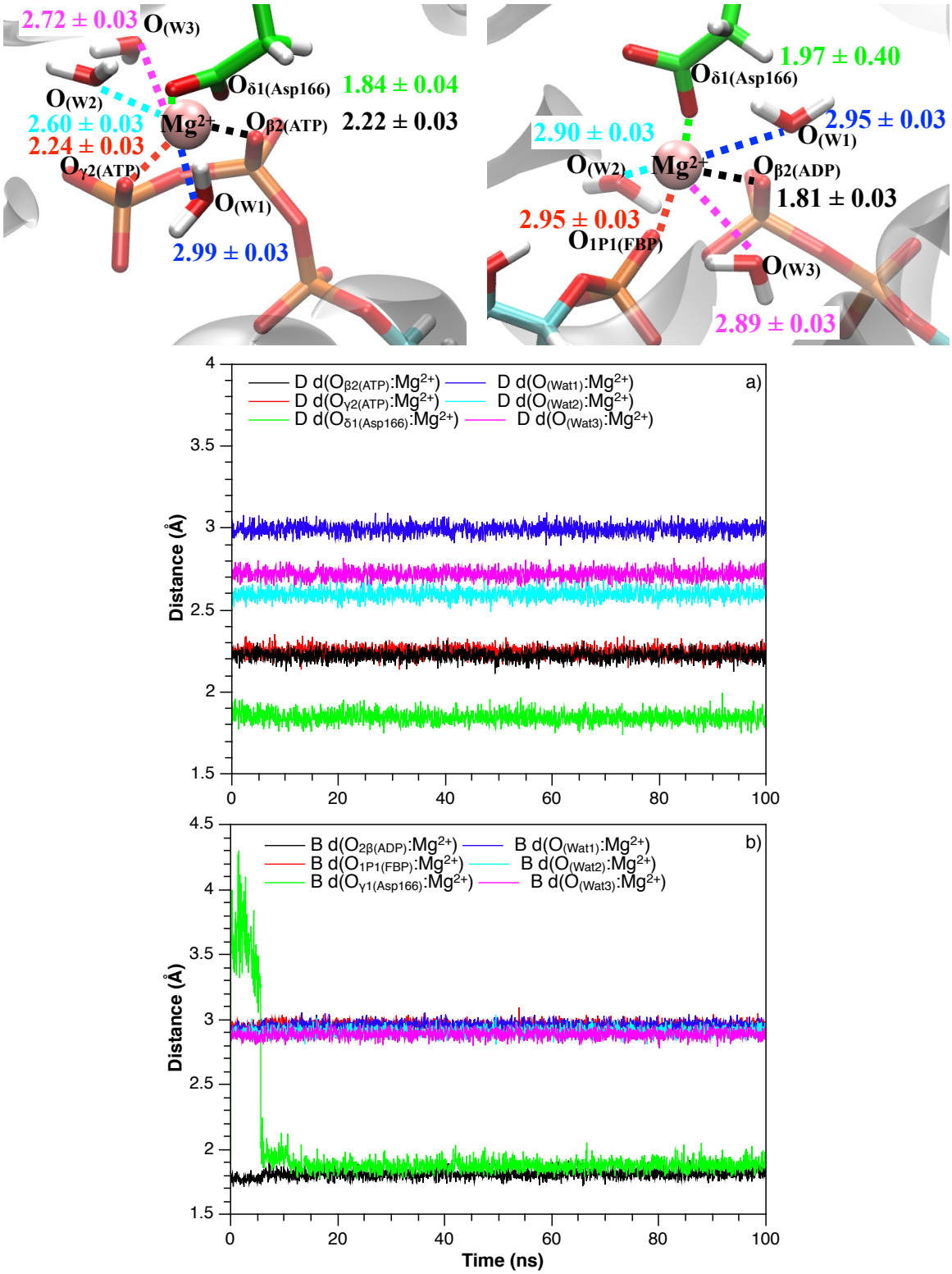

Fig. S8. Distance between Mg^{2+} ion and the atoms involved in its coordination sphere. (a) For chain D containing reactants and (b) for chain B containing products. The average distances from the simulation are also depicted, using the same color as in the legend.

5.3. Differences in the relative position between phosphoryl donor and acceptor in the active sites. The proper orientation of donor and acceptor ligands is critical for phosphoryl transfer catalysis. Some rearrangements that occurred in the interactions upon relaxation of the structure might affect the distance between the moieties that interchange the phosphoryl group. Therefore, the distance between ligands in each chain was measured considering the phospho-transfer acceptor oxygen in each case (O_1 of F6P and $O_3\beta$ of ADP for the active site containing reactants/products, respectively) and the phosphorus atom of the leaving (or transferred) phosphate group. As shown in Fig. S9, in the reactants-containing chain, the distance between ligands constantly fluctuated approximately 5.2 Å, but in the case of the chain containing products, this distance was more stable and remained constant at an average value of 4.3 Å in the last 40 ns.

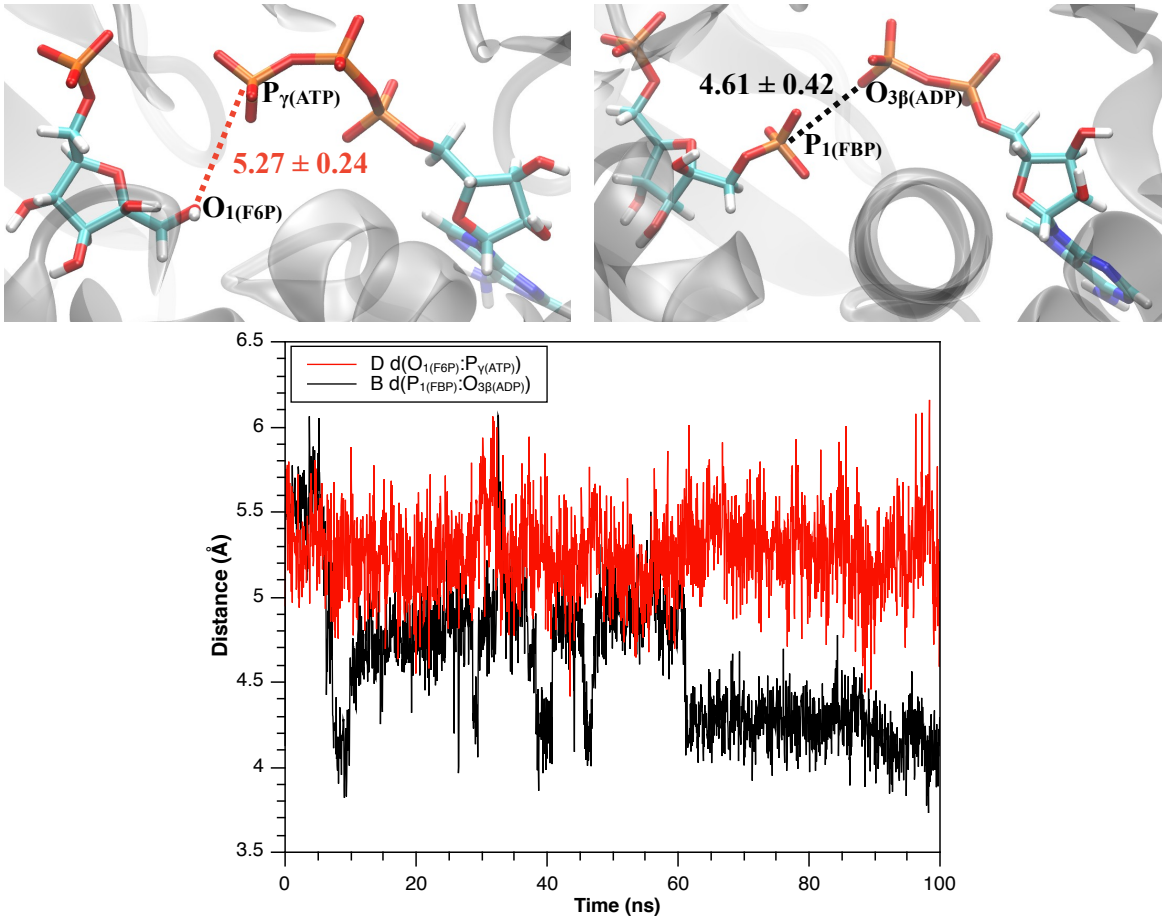

Fig. S9. Distance between ligands, considering the acceptor oxygen atom and the phosphorus atom of the leaving phosphate group for each chain. The chains are represented by letter B or D. The average distances from the simulation are also depicted, using the same color as in the legend.

6. The role of Lys27 in the converged mechanisms.

The upper part of Fig. S10 shows the evolution along the MFEP of the distance between the nitrogen atom of the ε-amino group of Lys27 ($N_{Z(Lys27)}$) and the phosphorous atom of the γ-phosphate of $MgATP^{2-}$ ($P\gamma_{(ATP)}$) for both converged pathways. In the lower part of Fig. S10, the percentage of frames with a HB found between these two groups was collected for both Paths as a function of the advance along the MFEP. Phosphate and proton transfer events are marked using dashed and pointed lines, respectively. A completely different behavior was observed for Path 1 and Path 2. In Path 1, where the phosphate transfer occurs first, Lys27 approaches one of the γ-phosphate oxygens, reaching a HB distance before the transition state was formed. The initial distance between $N_{Z(Lys27)}$ and $P\gamma_{(ATP)}$ is around 5.7 Å, but as the reaction moves forward this distance started to decrease until s = 0.4 (see Fig. S10a) at which the phosphate transfer occurred. This behavior pointed out the importance of this interaction, which assists the charge stabilization of the transferred phosphate in this mechanism. That is, the negative charge of the transferred group is stabilized by the positively charged Lys27, as is common for dissociative phosphoryl transfer mechanisms.[41] The percentage of HB configurations between $N_{Z(Lys27)}$ and $P\gamma_{(ATP)}$ (Fig. S10c) started to increase around s = 0.4 in Path 1, reaching its maximum value at s = 0.8. However, along Path 2, this residue stayed close to F6P, and only when the phosphate group was almost completely transferred, Lys27 started to have an HB interaction with it (see Fig. S10d). For Path 2, the distance between Lys27 and the protonated phosphate was substantially longer until s = 0.8 at which the final phosphate transfer event occurs (see Fig. S10b). This behavior suggests a minor role of this positively charged residue in the first stages of this mechanism; it must be recalled that in Path 2, the transferred phosphate group is protonated at the beginning of the process and thus its charge is reduced. Thus, the nature of the preferred reaction mechanism is strongly coupled to the conformational diversity of the enzymatic active site and, in particular, to the electrostatic complementarity between the reacting fragments (the transferred phosphate group) and the protein (Lys27).

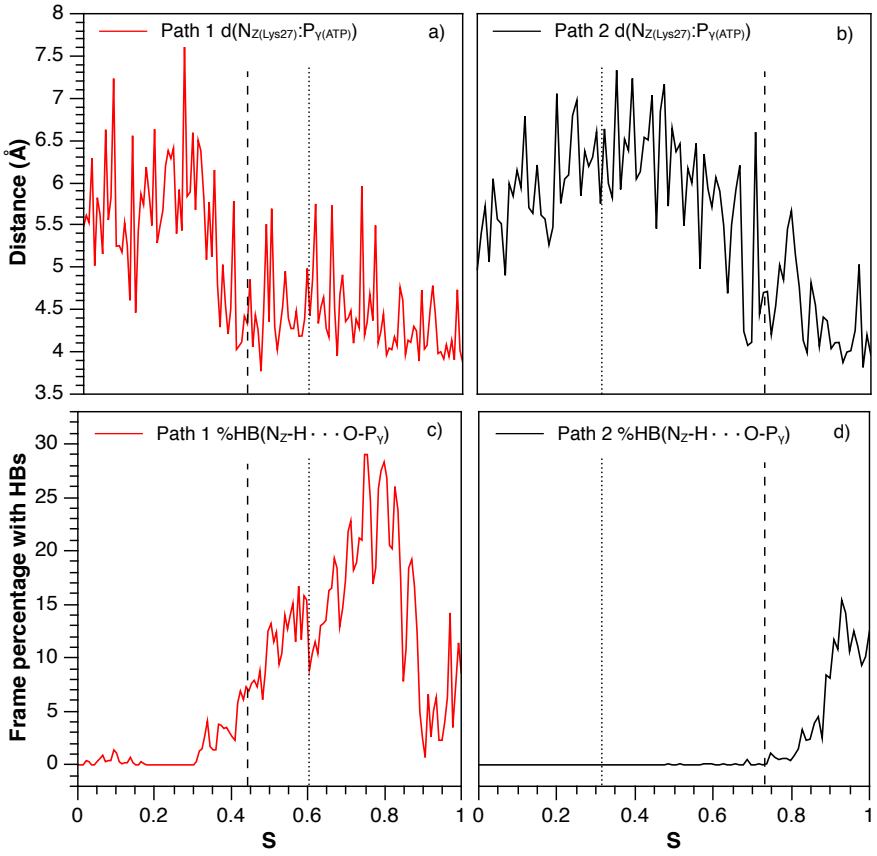

Fig. S10. Distances from the nitrogen atom of the ε-amino group from residue Lys27 to the phosphorus atom of the phosphosugar phosphate group obtained for Path 1 (a) and Path 2 (b) as a function of the collective path coordinates (*s*). Frame percentages with HBs found in Path 1 (c) and Path 2 (d) as a function of the collective path coordinates (*s*). The phosphate and proton transfer moments are indicated with dashed and pointed lines respectively.

7. Scan calculation linking both paths

In order to further investigate the relative energetics of Paths 1 and 2 and the possible dependence with respect to the chosen computational level, we performed an exploration of the potential energy surface at the B3LYP/MM level. In particular we carried out a relaxed B3LYP/MM scan along the tightness coordinate (the distance between the donor and acceptor oxygen atoms, $O_{3}\beta$-O_{1}) for structures where the phosphorous atom is equidistant to both oxygens. In this scan we moved the system from the dissociative pathway region (where the tightness coordinate takes values of around 5 Å) to the associative one (with values of about 4 Å for the tightness coordinate), see Figure S11. Our results clearly demonstrate that the associative pathway (Path 2) presents relative energies that would be 15-20 kcal·mol^{-1} larger than for the dissociative mechanism (Path 1), in good agreement with the difference observed between the activation free energies.

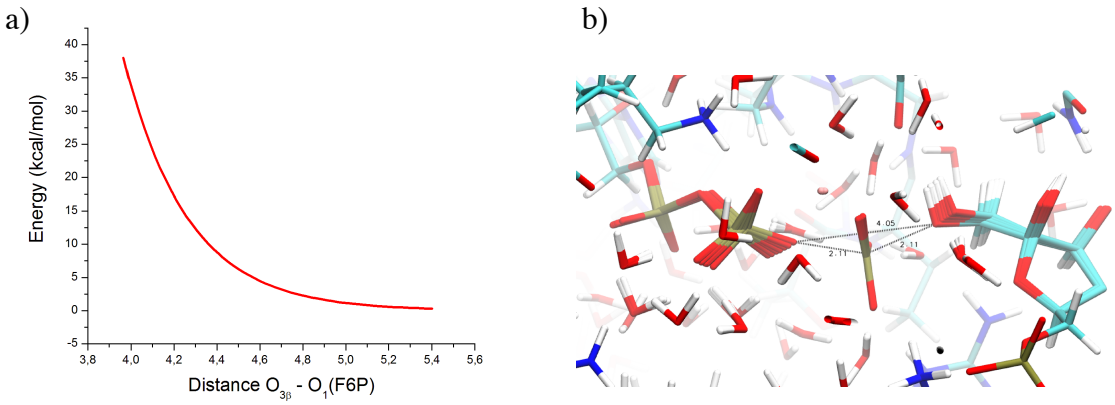

Fig. S11. (a) Scan calculation at the B3LYP/6-31G* level exhibiting the relative energy difference as a function of the $O_{3}\beta$-O_{1}(F6P) distance (values in Å) for structures where the phosphate group is equidistant between the donor and acceptor atoms. (b) Superposition of seven structures from the scan calculation showing the variation in the $O_{3}\beta$-P_{γ} and P_{γ}-O_{1}(F6P) distances (right). As an example, the distance of the last point of the scan is shown.

8. Testing free energy profile corrections

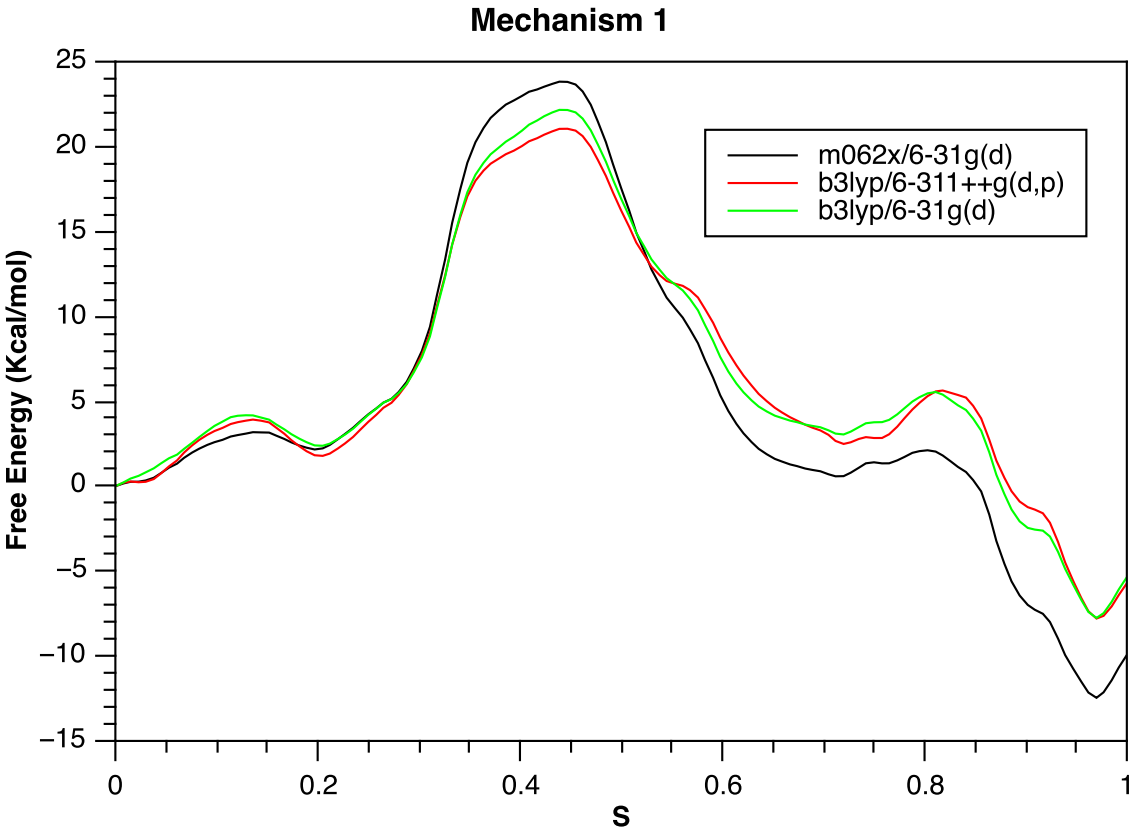

Fig. S12. Corrected free energy profile for Path 1 using different theoretical levels (see legend).

References

1 L. Miallau, W. N. Hunter, S. M. McSweeney and G. A. Leonard, *Journal of Biological Chemistry*, 2007, **282**, 19948–19957.

2 R. E. Parducci, R. Cabrera, M. Baez and V. Guixé, *Biochemistry*, 2006, **45**, 9291–9299.

3 W. Kabsch, *Acta Crystallographica Section D Biological Crystallography*, 2010, **66**, 125–132.

4 A. J. McCoy, R. W. Grosse-Kunstleve, P. D. Adams, M. D. Winn, L. C. Storoni and R. J. Read, *Journal of Applied Crystallography*, 2007, **40**, 658–674.

5 P. D. Adams, R. W. Grosse-Kunstleve, L. W. Hung, T. R. Ioerger, A. J. McCoy, N. W. Moriarty, R. J. Read, J. C. Sacchettini, N. K. Sauter and T. C. Terwilliger, *Acta Crystallogr. D Biol. Crystallogr.*, 2002, **58**, 1948–1954.

6 P. Emsley and K. Cowtan, *Acta Crystallographica Section D Biological Crystallography*, 2004, **60**, 2126–2132.

7 R. A. Laskowski, M. W. MacArthur, D. S. Moss and J. M. Thornton, *Journal of Applied Crystallography*, 1993, **26**, 283–291.

8 I. W. Davis, L. W. Murray, J. S. Richardson and D. C. Richardson, *Nucleic Acids Research*, 2004, **32**, W615–W619.

9 *Maestro, version 9.8*, Schrödinger, LLC, New York, NY, 2014.

10 M. H. M. Olsson, C. R. Søndergaard, M. Rostkowski and J. H. Jensen, *Journal of Chemical Theory and Computation*, 2011, **7**, 525–537.

11 H. J. C. Berendsen, J. P. M. Postma, W. F. van Gunsteren and J. Hermans, *Interaction models for water in relation to protein hydration, in `Intermolecular Forces'*, D. Reidel Publishing Company, Dordrecht, B. Pullman., 1981.

12 *Desmond Molecular Dynamics System, version 3.8*, D. E. Shaw Research, New York, NY, 2014.

13 *Maestro-Desmond Interoperability Tools, version 3.8*, Schrödinger, LLC, New York, NY, 2014.

14 D. Shivakumar, J. Williams, Y. Wu, W. Damm, J. Shelley and W. Sherman, *Journal of Chemical Theory and Computation*, 2010, **6**, 1509–1519.

15 J. L. Banks, H. S. Beard, Y. Cao, A. E. Cho, W. Damm, R. Farid, A. K. Felts, T. A. Halgren, D. T. Mainz, J. R. Maple, R. Murphy, D. M. Philipp, M. P. Repasky, L. Y. Zhang, B. J. Berne, R. A. Friesner, E. Gallicchio and R. M. Levy, *Journal of Computational Chemistry*, 2005, **26**, 1752–1780.

16 G. J. Martyna, M. L. Klein and M. Tuckerman, *The Journal of Chemical Physics*, 1992, **97**, 2635.

17 G. J. Martyna, D. J. Tobias and M. L. Klein, *The Journal of Chemical Physics*, 1994, **101**, 4177.

18 U. Essmann, L. Perera, M. L. Berkowitz, T. Darden, H. Lee and L. G. Pedersen, *The Journal of Chemical Physics*, 1995, **103**, 8577.

19 M. Tuckerman, B. J. Berne and G. J. Martyna, *The Journal of Chemical Physics*, 1992, **97**, 1990.

20 V. Kräutler, W. F. van Gunsteren and P. H. Hünenberger, *Journal of Computational Chemistry*, 2001, **22**, 501–508.

21 K. Nam, Q. Cui, J. Gao and D. M. York, *Journal of Chemical Theory and Computation*, 2007, **3**, 486–504.
22 E. Marcos, J. M. Anglada and R. Crehuet, *Physical Chemistry Chemical Physics*, 2008, **10**, 2442.
23 M. J. Field, M. Albe, C. Bret, F. Proust-De Martin and A. Thomas, *Journal of Computational Chemistry*, 2000, **21**, 1088–1100.
24 W. L. Jorgensen, D. S. Maxwell and J. Tirado-Rives, *Journal of the American Chemical Society*, 1996, **118**, 11225–11236.
25 U. C. Singh and P. A. Kollman, *Journal of Computational Chemistry*, 1986, **7**, 718–730.
26 M. J. Field, P. A. Bash and M. Karplus, *Journal of Computational Chemistry*, 1990, **11**, 700–733.
27 K. Zinovjev, J. J. Ruiz-Pernía and I. Tuñón, *Journal of Chemical Theory and Computation*, 2013, **9**, 3740–3749.
28 G. M. Torrie and J. P. Valleau, *Journal of Computational Physics*, 1977, **23**, 187–199.
29 A. D. Becke, *The Journal of Chemical Physics*, 1993, **98**, 5648–5652.
30 C. Lee, W. Yang and R. G. Parr, *Physical Review B*, 1988, **37**, 785–789.
31 S. H. Vosko, L. Wilk and M. Nusair, *Canadian Journal of Physics*, 1980, **58**, 1200–1211.
32 P. J. Stephens, F. J. Devlin, C. F. Chabalowski and M. J. Frisch, *The Journal of Physical Chemistry*, 1994, **98**, 11623–11627.
33 M. J. Frisch, G. W. Trucks, H. B. Schlegel, G. E. Scuseria, M. A. Robb, J. R. Cheeseman, G. Scalmani, V. Barone, G. A. Petersson, H. Nakatsuji, X. Li, M. Caricato, A. Marenich, J. Bloino, B. G. Janesko, R. Gomperts, B. Mennucci, H. P. Hratchian, J. V. Ortiz, A. F. Izmaylov, J. L. Sonnenberg, D. Williams-Young, F. Ding, F. Lipparini, F. Egidi, J. Goings, B. Peng, A. Petrone, T. Henderson, D. Ranasinghe, V. G. Zakrzewski, J. Gao, N. Rega, G. Zheng, W. Liang, M. Hada, M. Ehara, K. Toyota, R. Fukuda, J. Hasegawa, M. Ishida, T. Nakajima, Y. Honda, O. Kitao, H. Nakai, T. Vreven, K. Throssell, J. A. Montgomery, Jr., J. E. Peralta, F. Ogliaro, M. Bearpark, J. J. Heyd, E. Brothers, K. N. Kudin, V. N. Staroverov, T. Keith, R. Kobayashi, J. Normand, K. Raghavachari, A. Rendell, J. C. Burant, S. S. Iyengar, J. Tomasi, M. Cossi, J. M. Millam, M. Klene, C. Adamo, R. Cammi, J. W. Ochterski, R. L. Martin, K. Morokuma, O. Farkas, J. B. Foresman and D. J. Fox, *Gaussian 09*, Gaussian, Inc., Wallingford CT, 2016.
34 K. N. Houk, S. M. Gustafson and K. A. Black, *Journal of the American Chemical Society*, 1992, **114**, 8565–8572.
35 Huheey, *The Strengths of Chemical Bonds*, Butterworths, London, 2nd edn., 1958, vol. National Bureau of Standards.
36 S. Falsafi-Zadeh, Z. Karimi and H. Galehdari, *Bioinformation*, 2012, **8**, 341–343.
37 R. Cabrera, J. Babul and V. Guixé, *Archives of Biochemistry and Biophysics*, 2010, **502**, 23–30.
38 J. A. Sigrell, A. D. Cameron, T. A. Jones and S. L. Mowbray, *Structure*, 1998, **6**, 183–193.
39 Y. Zhang, M. Dougherty, D. M. Downs and S. E. Ealick, *Structure*, 2004, **12**, 1809–1821.
40 P. Bork, C. Sander and A. Valencia, *Protein Science*, 2008, **2**, 31–40.

41 J. K. Lassila, J. G. Zalatan and D. Herschlag, *Annual Review of Biochemistry*, 2011, **80**, 669–702.